

# Observation of an exotic lattice structure in the transparent $\text{KTa}_{1-x}\text{Nb}_x\text{O}_3$ perovskite supercrystal

Leonardo Lo Presti,<sup>1</sup> Jacopo Parravicini,<sup>2,\*</sup> Raffaella Soave,<sup>3</sup> Gianbattista Parravicini,<sup>4</sup> Michele Mauri,<sup>2</sup> Laura Loconte,<sup>1</sup> Fabrizio Di Mei,<sup>5</sup> Ludovica Falsi,<sup>5,6</sup> Luca Tartara,<sup>7</sup> Simona Binetti,<sup>2</sup> Aharon J. Agranat,<sup>8</sup> and Eugenio DelRe<sup>5</sup>

<sup>1</sup>*Dipartimento di Chimica, Università degli Studi di Milano, I-20133 Milano, Italy*

<sup>2</sup>*Dipartimento di Scienza dei Materiali, Università di Milano-Bicocca, I-20125 Milano, Italy*

<sup>3</sup>*Istituto di Scienze e Tecnologie Chimiche "Giulio Natta" (SCITEC), Italian CNR, I-20133 Milano, Italy*

<sup>4</sup>*Dipartimento di Fisica, Università di Pavia, I-27100 Pavia, Italy*

<sup>5</sup>*Dipartimento di Fisica, "Sapienza" Università di Roma, I-00185 Roma, Italy*

<sup>6</sup>*Dipartimento S.B.A.I., Sezione di Fisica, "Sapienza" Università di Roma, I-00161 Roma, Italy*

<sup>7</sup>*Dipartimento di Ingegneria Industriale e dell'Informazione, Università di Pavia, I-27100 Pavia, Italy*

<sup>8</sup>*Applied Physics Department, Hebrew University of Jerusalem, IL-91904 Jerusalem, Israel*

(Dated: December 10, 2020)

## SINGLE-CRYSTAL X-RAY DIFFRACTION

*Selection of single crystals.* The starting batch consisted of a transparent, hard and brittle mm-long rod of the freshly-synthesized KTN material. The rod was covered by some drops of inert perfluorinated oil to absorb as much as possible any mechanical stress. Then, its opposite extremities were cut with a stainless steel microblade. Irregular crystals of  $\mu\text{m}$  dimensions were obtained. Twelve of them were discarded after preliminary checks due to heavy twinning. In KTN, twinning is epitaxial (no indications of merohedry) and different for different specimens; moreover, larger (mm-sized) samples have greater chances to be heavily twinned. All these evidences indicate that differently oriented crystallites stem from defects originating during the crystal growth process and are not related to reorganization of ferroelectric domains. This is indeed a very common phenomenon when cubic high-symmetry materials are crystallized [1, 2]. Moreover, X-ray diffraction provides an atomic-resolution ( $\sim \text{nm}$  scale) average structural model from the whole volume of the crystal. The ferroelectric domain structure, whose symmetry -if any- is operational over a much larger length scale ( $\sim \mu\text{m}$ ), does not induce any macroscopic twinning. Would not this be the case, we would have detected clear evidences in diffraction images. Eventually, two high-quality non-pleochroic specimens were found, labelled as "A" and "B". Their dimensions not exceeded  $100 \mu\text{m}$  to alleviate the very high absorption of KTN ( $\mu \simeq 29.9 \text{ mm}^{-1}$ ) at the X-rays wavelength here employed ( $\lambda = 0.71073 \text{ \AA}$ ). Each crystal was mounted on the top of a glass capillary fiber with bicomponent epoxy glue and placed in very close proximity of the cold nitrogen nozzle. Then, diffraction data were acquired according to specs shown in the main text.

*Data collection strategy.* See Figure S-1 for a visual explanation of the diffractometer angles.

Diffraction amplitudes were collected in the  $\omega$ -scan mode (area detector fixed at  $2\theta = 0^\circ$ , sample rotating

around the goniometer  $z$ -axis by varying  $\omega$ ) and the temperature was changed stepwise from 295 K to 100 K, with  $\Delta T = 5 \text{ K}$ ; before starting any data acquisition, the sample was equilibrated in the cold  $\text{N}_2$  stream for  $\simeq 10'$ . After having completed the whole set of data acquisitions and having brought the crystal back to room temperature, we cooled it down again to  $T = 205 \text{ K}$ ,  $155 \text{ K}$  and  $110 \text{ K}$ . Upon 6 to 20 hrs of equilibration under the cold  $\text{N}_2$  stream, the diffraction experiments were repeated. The corresponding estimates for the cell parameters were identical to the previous ones within the least-squares error (Figure S-2), confirming the lacking of hysteresis phenomena and the full thermal equilibration of the crystal during the previous  $T$  scan.

The same hemisphere of data was sampled up to a maximum Bragg angle of  $\simeq 37^\circ$  throughout the whole 100 K - room-temperature range of  $T$ , invariably providing a number of single measurements per experiment ranging from 104 to 112 for the "A" specimen (Table S-I). Lattice constants were computed by minimizing the average square deviations between the measured positions of intense reflections and those predicted on the basis of the structural model. In the standard procedure, lattice constants are varied together with instrumental parameters, which include possible detector misplacements and centering errors of the crystal. In KTN,  $T$ -driven distortions of cell edge lengths are very small ( $\leq 0.1\%$ ), and of the same order of magnitude as the least-squares estimated adjustments affecting the instrumental parameters. This results in high correlations, which imply an odd dependence of the instrumental parameters on the cell edges and vice-versa, as well as very high estimated standard deviations of the final least-squares variables.

To limit these problems, we measured the positions of the Bragg peaks in the reciprocal reference frame using a very small scan width in  $\omega$  ( $\Delta\omega = 0.15^\circ$ ). Possible systematic errors in the position of the instrumental zero were minimized by collecting reflections at both positive and negative  $2\theta$ . Finally, fast exposure times (3 s/frame)

were used to ensure that counting statistics always remain in the linearity region of the CCD detector device. This way, the diffraction maxima can be accurately located, even for the most intense reflections.

On the least-squares side, a preliminary optimization of the instrumental parameters was carried out against the room temperature data of both the “A” and “B” specimens. Cell edge lengths and angles were repeatedly refined at fixed values of the instrumental parameters. Eventually, the set of instrumental parameters corresponding to lattice constants in fair agreement with Literature estimates ( $a = 3.99279 \text{ \AA}$ ) [3] was deemed as the least biased one and kept fixed in all the subsequent refinements down to 100 K. As both the detector position and the sample mounting were never changed for a whole set of experiments down to 100 K and back to RT, such parameters are indeed not expected to vary [37], and the choice of keeping them fixed, once optimized, is fully justified. Moreover, no symmetry constraints were imposed all over the whole procedure. The lattice constants were always refined in the triclinic system, without any preconceived selection of expected symmetries. Deviations of cell angles from  $90^\circ$  were irregular and always very small ( $\leq 0.02^\circ$ ) throughout the whole range of  $T$  (Figure S-3). As regards to the rhombohedral phase, it is characterized by the presence of a 3rd-order symmetry axis, which is compatible with our structural model. It is true that cell angles in a rhombohedral cell must fulfil  $\alpha = \beta = \gamma \neq 90^\circ$ , but in KTN the lattice distortions are very small and the corresponding precision on cell angles quite poor in terms of least-squares estimated standard deviations. No certain trends can be deduced from Fig. S-3, apart from a tendency towards lower symmetry upon cooling. On the contrary, the precision on cell edge lengths is sufficient to extract meaningful structural data (Fig. 1). Below 130 K, the three cell edges become equal to their average length within 1 estimated standard deviation ( $a = b = c$ ). While this is compatible also with a cubic symmetry, with equal cell edges and angles of  $90^\circ$ , but it is more likely that we have a rhombohedral phase, whose distortion from the cubic shape is too small to be detectable with the current precision of cell angles estimate. This view is consistent with both the Literature, which describes the low- $T$  phase of KTN-type materials as rhombohedral, and the reduction of point symmetry that we expect for translationengleiche-kind phase transitions between the RT and lowest- $T$  phases.

It is worth stressing that the present single crystal X-ray estimates of the KTN lattice parameters come from the accurately determined positions of more than one hundred intense reflections, uniformly distributed in the reciprocal lattice. Despite least-squares averaging of unit cell parameters and very small distortions of the KTN cell (Fig. 1A in the main text and Figure S-5), our structural model is able to unequivocally locate statistically different regions of anomalous response. We do reproduce

not only all the (1)-(3) first-order transitions detected by DSC (Fig. 3A in the main text and Figure S-7), but we also obtain a strict quantitative agreement of phase transition temperatures with the dielectric measurements (Fig. 3 in the main text and Figures S-8, S-11). This secures the accuracy of the method above described.

## TREND OF CELL PARAMETERS

*Comment on the unit cell distortions.* Figure 1A (main text) and Figure S-3 show the behavior of lattice parameters of the specimens “A” and “B”, cut from the opposite side of the original KTN rod, as a function of  $T$  (Figure S-2). The corresponding tabular entries can be found in Table S-I and S-II below. To date, accurate descriptions of  $T$ -driven lattice distortions in perovskite relaxors are scanty and restricted to a few compounds [4–9]. X-ray [10] and neutron [11] diffraction experiments usually rely on few selected Bragg reflections, and do not detect significant distortions from the average cubic symmetry down to very low  $T$  [12]. By means of accurately designed diffraction experiments (see below), we monitored 100+ intense Bragg reflections as a function of  $T$ , down to 100 K. The diffraction data were uniformly distributed in the reciprocal lattice up to  $\max[\sin(\theta)/\lambda] = 0.45 \text{ \AA}^{-1}$  (see below), and each of them represents the scattering output from the entire volume of the bulk material. We were thus able to measure very precisely the cell edge length down to 100 K, obtaining for the first time reliable estimates of the  $T$ -driven lattice distortions in KTN.

Unexpectedly, the symmetries of the low- $T$  KTN phases do not conform to those reported for the prototypical  $\text{BaTiO}_3$  perovskite (cubic-tetragonal-orthorhombic-trigonal). Actually, an orthorhombic phase appears just a few degrees below the Curie temperature, and then it is followed by two distinct tetragonal phases that eventually transform into a rhombohedral one. The main transitions (Fig. 1A and Fig. 3A in the main text) are not sample-dependent and are clearly associated to first-order phenomena, with neat latent heats and significant changes in the dielectric permittivity (Fig. 3B,C in the main text). We note, though, that allegedly second-order transitions are also present, whose exact boundaries depend on the thermodynamic history of the sample (see also Fig.S-5). A full characterization of the phase diagram of KTN as a function of  $T$  will be the topic of future studies.

The orthorhombic anomaly also implies a strongly anisotropic thermal response. Analogously to  $\text{BaTiO}_3$  [13], KTN undergoes a negative thermal expansion (NTE) along the  $c$ -axis between 232 and 287 K, with a linear expansion coefficient  $\alpha_p(c) = -1.95(1) \cdot 10^{-5} \text{ K}^{-1}$  (sample “A”, Fig. 1 of main text). As the other two axes show ordinary positive thermal expansion, the distortion of the cell volume is three orders of magnitude lower (Ta-

bles S-I-S-II), with  $\alpha_p(V) = +1.78(1) \cdot 10^{-8} K^{-1}$  for the sample “A”. A similar NTE behavior, though implying a larger distortion of the whole cell, was observed in perovskite oxides undergoing first-order phase transitions, such as  $\text{Bi}_{0.95}\text{La}_{0.05}\text{NiO}_3$ , where a gradual reduction of the cell volume occurs above  $T = 320$  K due to a polarization-induced spontaneous charge transfer from Ni to Bi [14]. In  $\text{KTa}_{1-x}\text{Nb}_x\text{O}_3$  materials, it has been reported [10] that a molar amount of Nb of  $x = 0.011$  can trigger a neat NTE response for the whole unit cell, but only at very low temperatures (30 K). In our KTN sample, an anisotropic NTE occurs very close to room temperature, being related to the appearing of the polar 4mm phase. Thus, the thermodynamic driving force is likely some kind of spontaneous polarization of the lattice.

From a crystallographic viewpoint, the detected distortions of the average unit cell below  $T_C$  imply that the crystal field is significantly less symmetric than in the high- $T$  cubic phase, as it exploits different kind and amount of lattice strains along the three main reference axes (Fig. 1 in the main text). From dielectric spectroscopy measurements (see below) and light scattering experiments close to the Curie temperature (see the main text), it is clear that the 230 – 270K region is associated to organization phenomena of polarization domains at the mesoscopic scale.

Upon further cooling, a tetragonal phase appears below  $T \simeq 228$  K, with active  $c > a = b$  symmetry constraints. At  $T \simeq 182$  K, a tetragonal-to-tetragonal transition takes place, where the equality  $a = b$  still holds true, while a steep reduction of the  $c$  axis occurs (Fig. 1 in the main text and Figure S-5). Finally, below  $T \simeq 125$  K (Fig. 1A in the main text and Figure S-5), another transition occurs, which is not detected by differential scanning calorimetry (DSC). This last transition constrains the cell edges to become all equal to their average within 2 standard deviations. This is compatible with the  $a = b = c$  constraint typical of the trigonal ( $3m$ ) symmetry, as confirmed also by dielectric spectroscopy (see below).

The same first order transitions are found also in the “B” specimen at almost identical temperatures as in the “A” one. Those occurring without exchange of latent heat, on the contrary, are considerably downshifted at  $T \simeq 250$  K and  $\simeq 118$  K (Figure S-5) in the sample “B”. This suggests that they depend on the amount of defects, and indeed the axial microstrain of the two samples shows a different behaviour (Figure S-6, see below). In this case, the nucleation of the emerging phase should start at pre-existing grain boundaries or dislocations [15, 16]. Then, the topological phase is free to spread across the crystallite, up to its boundaries. Multiple nucleation events are required to complete the transition, which takes place over a certain range of  $T$ . Accordingly, a precise transition temperature cannot be defined, in fair agreement

with our experiments. Triebwasser [17] suggested that in  $\text{KTa}_x\text{Nb}_{1-x}\text{O}_3$ , the order of the ferroelectric transition should switch from the first to the second one when the concentration of Tantalum exceeds 55 %. At variance with him, we found that for  $x = 0.36$ , first-order phenomena exist.

*Comment to Figure S-6.* The thermal evolution of the axial ratio  $c/a$ , which is related to the lattice microstrain in the polar direction, is also sample-dependent. This parameter quantifies the magnitude of the distortion along the  $C_4$  polar axis in the ferroelectric phases. In the 220 K-room-temperature range, the axial strain is markedly higher in magnitude in “B” than in “A” sample. In other words, “B” undergoes a larger tetragonal distortion upon developing the ferroelectric phase, even though both crystals show a markedly similar trend at lower temperatures. A possible explanation resides in an allegedly greater amount of defects in “B” (see above), which implies a higher average microstrain upon symmetry breaking. Interestingly, when  $c$  enters the positive thermal expansion regime, the  $c/a$  ratio becomes essentially identical in both the specimens, possibly indicating that changes in the microstructure might reach a sort of saturation regime. This might be related in turn to the fact that lattice distortions are generally much lower in low- $T$  phases of KTN than in the high- $T$  ones.

## DIFFERENTIAL SCANNING CALORIMETRY

As seen in Fig. 3A in the main text, three well separated and clearly defined endothermic peaks are detected at  $T \simeq 182, 228$  and 285 K by performing differential scanning calorimetry (DSC) on the KTN crystals. Fig. S-7 exemplifies an experiment performed on a single crystal at a rate of 10 K/min. At this rate, the two lower temperature events appear as well defined 1<sup>st</sup> order transitions, while the transition at higher temperature is much broader. The correspondent latent heats [18] range from 0.12 to 0.25 J/g (Table S-IV), in agreement with literature [19]. During the cooling run, reverse transitions are visible but at slightly downshifted temperatures, thus reinforcing the assignment of the thermal events to first order phenomena [20]. Mismatch between heating and cooling onset of transition 1 is instead due to the breadth of the transition itself.

Slowing down the cooling/heating rates to 2 K/min confirmed the nature of transition (3), the one at lowest temperature, as a first order transition producing a single peak. The intermediate transition at  $T \simeq 228$  K instead splits into several partially convoluted peaks, indicating the occurrence of partially superimposed reorganization processes in the crystal.

The lowest- $T$  transition at 182 K maintains its breadth at all temperature rates. All onset temperatures are presented in Table S-III, together with integrated values as-

T	N <sup>a</sup>	a	b	c	$\alpha$	$\beta$	$\gamma$	V	$\sigma(a)^b$	$\sigma(b)^b$	$\sigma(c)^b$	$\sigma(\alpha)^b$	$\sigma(\beta)^b$	$\sigma(\gamma)^b$	$\sigma(V)^b$
295	111	3.9938	3.9943	3.9944	89.988	89.993	89.984	63.72	0.0003	0.0003	0.0003	0.005	0.005	0.006	0.01
290	112	3.9939	3.9942	3.9945	89.990	89.992	89.983	63.72	0.0003	0.0003	0.0002	0.005	0.005	0.005	0.01
285	112	3.9939	3.9941	3.9947	89.990	89.992	89.985	63.72	0.0003	0.0003	0.0002	0.005	0.005	0.005	0.01
280	109	3.9936	3.9936	3.9952	89.994	89.992	89.986	63.72	0.0003	0.0003	0.0002	0.005	0.005	0.005	0.01
275	108	3.9935	3.9934	3.9957	89.992	89.993	89.988	63.72	0.0003	0.0003	0.0002	0.005	0.005	0.005	0.01
270	108	3.9935	3.9931	3.9963	89.993	89.994	89.990	63.73	0.0003	0.0003	0.0002	0.005	0.005	0.005	0.01
265	107	3.9935	3.9928	3.9967	89.992	89.999	89.990	63.73	0.0003	0.0003	0.0002	0.005	0.005	0.005	0.01
260	106	3.9933	3.9926	3.9971	89.992	89.997	89.991	63.73	0.0003	0.0003	0.0002	0.005	0.005	0.005	0.01
255	107	3.9933	3.9924	3.9976	89.989	89.999	89.992	63.73	0.0002	0.0003	0.0002	0.005	0.005	0.005	0.01
250	108	3.9932	3.9920	3.9978	89.993	89.998	89.990	63.73	0.0003	0.0003	0.0002	0.005	0.005	0.005	0.01
245	106	3.9930	3.9918	3.9980	89.994	89.995	89.990	63.73	0.0003	0.0003	0.0002	0.005	0.005	0.005	0.01
240	109	3.9929	3.9913	3.9984	90.000	89.996	89.985	63.72	0.0003	0.0003	0.0002	0.005	0.005	0.005	0.01
235	107	3.9928	3.9913	3.9986	89.996	89.994	89.989	63.72	0.0002	0.0002	0.0002	0.005	0.005	0.005	0.01
230	104	3.9926	3.9910	3.9990	89.998	89.996	89.985	63.72	0.0003	0.0003	0.0002	0.005	0.005	0.005	0.01
225	107	3.9926	3.9920	3.9982	89.987	89.999	89.989	63.73	0.0003	0.0003	0.0002	0.005	0.005	0.005	0.01
220	106	3.9925	3.9923	3.9979	89.988	89.994	89.987	63.72	0.0003	0.0003	0.0002	0.005	0.005	0.005	0.01
215	106	3.9924	3.9925	3.9980	89.988	89.995	89.985	63.73	0.0003	0.0003	0.0002	0.005	0.005	0.005	0.01
210	104	3.9924	3.9923	3.9978	89.990	89.998	89.992	63.72	0.0003	0.0003	0.0002	0.005	0.005	0.005	0.01
205	105	3.9928	3.9925	3.9979	89.985	90.006	90.001	63.73	0.0003	0.0003	0.0003	0.007	0.006	0.006	0.01
200	107	3.9926	3.9925	3.9980	89.982	90.006	90.002	63.73	0.0003	0.0003	0.0003	0.006	0.006	0.006	0.01
195	107	3.9926	3.9923	3.9982	89.989	90.008	90.000	63.73	0.0003	0.0003	0.0003	0.007	0.006	0.007	0.01
190	108	3.9922	3.9923	3.9981	89.989	90.002	89.989	63.72	0.0003	0.0003	0.0002	0.005	0.005	0.005	0.01
185	108	3.9924	3.9923	3.9981	89.988	90.007	89.996	63.73	0.0003	0.0003	0.0003	0.006	0.006	0.006	0.01
180	108	3.9936	3.9919	3.9968	89.987	90.006	89.998	63.72	0.0003	0.0003	0.0003	0.006	0.006	0.006	0.01
175	109	3.9934	3.9928	3.9958	89.984	90.003	89.992	63.71	0.0003	0.0003	0.0002	0.005	0.005	0.005	0.01
170	109	3.9935	3.9931	3.9955	89.981	90.004	89.995	63.71	0.0003	0.0003	0.0002	0.005	0.005	0.005	0.01
165	107	3.9933	3.9931	3.9953	89.985	90.004	89.995	63.71	0.0003	0.0003	0.0003	0.006	0.005	0.006	0.01
160	110	3.9935	3.9932	3.9953	89.982	90.005	89.999	63.71	0.0003	0.0003	0.0002	0.005	0.005	0.005	0.01
155	107	3.9934	3.9933	3.9953	89.980	90.009	89.998	63.71	0.0003	0.0003	0.0002	0.005	0.005	0.006	0.01
150	107	3.9933	3.9931	3.9950	89.984	90.004	89.998	63.70	0.0003	0.0003	0.0003	0.005	0.005	0.006	0.01
145	107	3.9935	3.9932	3.9951	89.983	90.007	90.001	63.71	0.0003	0.0003	0.0003	0.005	0.005	0.006	0.01
140	107	3.9935	3.9932	3.9950	89.984	90.007	90.002	63.71	0.0003	0.0003	0.0003	0.006	0.005	0.006	0.01
135	106	3.9935	3.9933	3.9950	89.978	90.007	90.006	63.71	0.0003	0.0003	0.0003	0.006	0.005	0.006	0.01
130	106	3.9934	3.9931	3.9948	89.983	90.002	90.001	63.70	0.0003	0.0003	0.0003	0.006	0.005	0.006	0.01
125	107	3.9941	3.9935	3.9943	89.979	90.008	90.013	63.71	0.0003	0.0003	0.0003	0.006	0.006	0.006	0.01
120	107	3.9941	3.9934	3.9942	89.979	90.008	90.012	63.71	0.0003	0.0003	0.0003	0.006	0.006	0.006	0.01
115	107	3.9942	3.9933	3.9942	89.976	90.009	90.015	63.71	0.0003	0.0003	0.0003	0.006	0.006	0.006	0.01
110	109	3.9942	3.9934	3.9942	89.983	90.008	90.009	63.71	0.0003	0.0003	0.0003	0.006	0.006	0.006	0.01
105	108	3.9937	3.9931	3.9939	89.986	90.000	90.000	63.69	0.0003	0.0003	0.0003	0.006	0.005	0.006	0.01
100	109	3.9938	3.9932	3.9939	89.989	90.001	90.002	63.69	0.0003	0.0003	0.0003	0.006	0.005	0.006	0.01

<sup>a</sup>Number of reflections we employed in the least squares procedure.

<sup>b</sup>Estimated standard deviation.

TABLE S-I. Numerical values of lattice parameters and cell volumes of the KTN crystal “A” as a function of  $T$ , in K, Å, deg and Å<sup>3</sup>, as retrieved from single crystal X-ray diffraction. These data are reported in graphical form in Figure 1 of main text. Horizontal bars set the limits of the corresponding crystal phases.

sociated to each transition. For the 228K transition, we performed an overall integral for the measurement of the associated enthalpy since the different peaks were only apparent at the lowest rates, and partially convoluted.

From all the experiments, average values representative of the transitions are extracted, and approximated to  $\pm 1$  K.

*Comments to Table S-IV.* Enthalpy and entropy changes associated to transitions (2) and (3) are very similar in KTN and BaTiO<sub>3</sub>, indicating that similar microscopic processes likely provide an analogous thermodynamic drive in both the materials. Instead, across (1)  $\Delta S$  is lower in KTN than in BaTiO<sub>3</sub>, due to the higher enthalpy of this transition. This agrees well with the fact that very small cell distortions, which are associated to small enthalpic and entropic gains, occur in KTN.

## DIRECTIONAL DIELECTRIC SPECTROSCOPY

In Fig. S-8a, b, c the relative real permittivity as a function of temperature  $T$  is reported, for the employed frequencies of 1, 10, 100, 1000 kHz, along the crystalline axes  $a$ ,  $b$ , and  $c$  respectively, in the 20-300 K range, upon cooling. The  $\epsilon(T)$  curves, for all the investigated directions, point out the occurring of three main phase transitions. In particular the transitions are evidenced, for all the considered directions, by the manifestation of peaks of permittivity at  $T_m$  which, in our case, can be estimated at 288, 227, and 180 K. Transition peaks are coupled with the overlapping of the curves for the different frequencies in correspondence with a sharp variation of  $\epsilon(T)$ . They are few degrees spaced from the maxima so marking a further temperature (the Curie temperature,  $T_C$ ) distinguishing the transformation. This kind of feature is found in agreement with that reported in

T	N <sup>a</sup>	a	b	c	$\alpha$	$\beta$	$\gamma$	V	$\sigma(a)^b$	$\sigma(b)^b$	$\sigma(c)^b$	$\sigma(\alpha)^b$	$\sigma(\beta)^b$	$\sigma(\gamma)^b$	$\sigma(V)^b$
295	96	3.9938	3.9945	3.9938	90.010	90.010	89.995	63.714	0.0002	0.0003	0.0002	0.0005	0.005	0.005	0.01
290	94	3.9943	3.9933	3.9941	90.007	90.008	89.990	63.708	0.0002	0.0002	0.0002	0.004	0.004	0.004	0.01
285	95	3.9951	3.9932	3.9937	90.006	90.005	89.987	63.712	0.0002	0.0002	0.0002	0.004	0.004	0.004	0.01
280	97	3.9968	3.9929	3.9933	90.003	90.012	89.990	63.728	0.0002	0.0002	0.0002	0.005	0.005	0.005	0.01
275	97	3.9975	3.9928	3.9930	90.003	90.013	89.992	63.733	0.0002	0.0002	0.0002	0.004	0.004	0.004	0.01
270	96	3.9980	3.9923	3.9923	90.010	90.009	89.994	63.722	0.0002	0.0002	0.0002	0.004	0.004	0.004	0.01
265	96	3.9984	3.9921	3.9920	90.005	90.009	89.991	63.720	0.0002	0.0002	0.0002	0.004	0.004	0.004	0.01
255	97	3.9998	3.9911	3.9910	90.008	90.005	89.990	63.711	0.0002	0.0002	0.0002	0.004	0.004	0.004	0.01
245	97	3.9998	3.9915	3.9906	90.011	90.003	89.986	63.711	0.0002	0.0002	0.0002	0.004	0.004	0.004	0.01
235	95	4.0006	3.9913	3.9903	90.007	90.006	89.992	63.715	0.0002	0.0002	0.0002	0.004	0.004	0.004	0.01
230	96	4.0007	3.9912	3.9902	90.010	90.006	89.988	63.714	0.0002	0.0002	0.0002	0.004	0.004	0.004	0.01
225	98	4.0003	3.9909	3.9909	90.005	90.003	89.988	63.714	0.0002	0.0002	0.0002	0.004	0.004	0.004	0.01
220	97	3.9978	3.9925	3.9917	90.007	89.996	89.987	63.712	0.0002	0.0002	0.0002	0.004	0.004	0.004	0.01
200	99	3.9975	3.9923	3.9922	90.005	89.996	89.986	63.712	0.0002	0.0002	0.0002	0.004	0.004	0.004	0.01
190	95	3.9972	3.9923	3.9919	90.003	89.996	89.991	63.703	0.0002	0.0002	0.0002	0.004	0.004	0.004	0.01
185	95	3.9971	3.9924	3.9917	90.004	89.996	89.986	63.700	0.0002	0.0002	0.0002	0.004	0.004	0.004	0.01
180	95	3.9967	3.9932	3.9920	90.002	90.000	89.992	63.711	0.0002	0.0002	0.0002	0.004	0.004	0.004	0.01
175	98	3.9953	3.9933	3.9931	90.005	89.994	89.989	63.708	0.0002	0.0002	0.0002	0.004	0.004	0.004	0.01
170	98	3.9948	3.9934	3.9930	90.010	89.990	89.986	63.700	0.0002	0.0002	0.0002	0.004	0.004	0.004	0.01
160	96	3.9947	3.9934	3.9931	90.006	89.987	89.990	63.700	0.0002	0.0002	0.0002	0.004	0.003	0.003	0.01
150	97	3.9945	3.9934	3.9931	90.005	89.988	89.991	63.696	0.0002	0.0002	0.0002	0.003	0.003	0.003	0.01
140	94	3.9942	3.9935	3.9930	90.006	89.982	89.993	63.692	0.0002	0.0002	0.0002	0.004	0.004	0.004	0.01
135	95	3.9944	3.9935	3.9932	90.008	89.983	89.997	63.698	0.0002	0.0002	0.0002	0.004	0.004	0.004	0.01
130	96	3.9943	3.9935	3.9932	90.006	89.980	89.996	63.696	0.0002	0.0002	0.0002	0.003	0.003	0.003	0.01
125	96	3.9941	3.9934	3.9929	90.006	89.977	89.998	63.687	0.0002	0.0002	0.0002	0.003	0.003	0.003	0.01
120	96	3.9942	3.9935	3.9931	90.010	89.978	89.995	63.693	0.0002	0.0002	0.0002	0.003	0.003	0.003	0.01
115	96	3.9940	3.9936	3.9930	90.007	89.974	90.002	63.690	0.0002	0.0002	0.0002	0.004	0.004	0.004	0.01
110	96	3.9943	3.9937	3.9928	90.006	89.978	89.999	63.693	0.0002	0.0002	0.0002	0.004	0.004	0.004	0.01
105	97	3.9943	3.9938	3.9929	90.007	89.979	90.002	63.696	0.0002	0.0002	0.0002	0.003	0.003	0.003	0.01
100	97	3.9942	3.9937	3.9929	90.006	89.977	89.998	63.693	0.0002	0.0002	0.0002	0.003	0.003	0.003	0.01

<sup>a</sup>Number of reflections we employed in the least squares procedure.

<sup>b</sup>Estimated standard deviation.

TABLE S-II. Same as Table S-I for the “B” crystal.

DSC Rate (K)	Transition 3		Transition 2		Transition 1		DH(abs) kJ/mol	DS (J/mol*K)	Onset (K)	DH (J/g)	DH(abs) kJ/mol	DS (J/mol*K)
	Onset (K)	DH (J/g)	DH(abs) kJ/mol	DS (J/mol*K)	Onset (K)	DH (J/g)						
10	186.33	-0.10	0.024	0.13	227.97	-0.22	0.052	0.23	281.76	-0.30	0.071	0.25
-10	178.56	0.14	0.033	0.19	228.66	0.22	0.052	0.23	288.4	0.27	0.064	0.22
10	186.31	-0.11	0.026	0.14	227.86	-0.24	0.057	0.25	281.53	-0.34	0.080	0.29
-10	178.29	0.15	0.035	0.20	228.49	0.26	0.061	0.27	289	0.44	0.104	0.36
10	187.15	-0.10	0.024	0.13	227.6	-0.22	0.052	0.23	281.45	-0.45	0.106	0.38
-10	177.67	0.14	0.033	0.19	228.56	0.24	0.057	0.25	289.02	0.41	0.097	0.34
5	186.83	-0.13	0.031	0.16	228.41	-0.20	0.047	0.21	281.88	-0.37	0.087	0.31
-5	176.89	0.13	0.031	0.17	228.32	0.23	0.054	0.24	289.17	0.43	0.102	0.35
15	185.84	-0.21	0.050	0.27	228.58	-0.23	0.054	0.24	280.86	-0.42	0.099	0.35
-15	178.34	0.13	0.031	0.17	229.01	0.23	0.054	0.24	289.41	0.44	0.104	0.36
2	187.3	-0.12	0.028	0.15	228.7	-0.23	0.054	0.24	279.84	-0.33	0.078	0.28
-2	177.38	0.12	0.028	0.16	228.05	0.21	0.050	0.22	288.36	0.26	0.061	0.21
Average	182.24		0.03	0.17	228.35		0.05	0.24	285.06		0.09	0.31

TABLE S-III. Thermodynamic parameters retrieved from the integration of the DSC. Positive rates indicate heating runs, while negative rates indicate cooling runs.

Transition	KTN			BaTiO <sub>3</sub>		
	Onset $T$ (K)	$\Delta H$ (kJ/mol)	$\Delta S$ (J/mol K)	Peak $T$ (K)	$\Delta H$ (kJ/mol)	$\Delta S$ (J/mol K)
(1)	285	0.088	0.31	$\simeq 393$	0.1965	0.50
(2)	228	0.054	0.24	$\simeq 278$	0.0583	0.21
(3)	182	0.030	0.17	$\simeq 183$	0.0311	0.17

TABLE S-IV. Thermodynamic parameters retrieved from the integration of the DSC (see Figure 3 in the main text) of  $\text{KTa}_{0.64}\text{Nb}_{0.36}\text{O}_3$  (molecular weight: 236.35 g/mol, peaks on cooling). Comparison with the same quantities derived from the prototypical barium titanate material by Shirane & Takeda is also given [18].

the literature on lead free relaxor ferroelectrics [4, 21–23]: it is worth noting that our sample presents the features of a sharp-transition relaxor, with  $T_C < T_m$  (see Fig. 9 of [4]). Actually, the difference between  $T_m$  and  $T_C$  can be assumed as an estimation of the temperature amplitude of the considered transition, whose largest extension is shown by the lowest temperature transformation (in agreement with the X-ray results). As depicted in the inset of Figure S-8a, lowering temperature below the above-mentioned lowest transition, the permittivity curves show along the  $a$ -direction a clear feature of instability starting at 115 K and subsequently a peak centered at 110 K is found and a change of the  $\epsilon(T)$  curves slope is also observed. Such a kind of response, although it is different in shape and intensity with respect to that of the above-considered transformations, can be associated with the occurring structural variation mainly  $a$ -direction related. Finally, below 110 K to the lowest measured temperature 20 K,  $\epsilon(T)$  shows a quite regular behavior that is peculiar of a stable phase. Such an interpretation is confirmed by the transition at 125 K detected by X-ray diffractometry (see Fig. 1A of the main text).

## FRÖHLICH ENTROPY

The analysis of the evolution in temperature of the perovskite sample state of order, which has shown a key factor in several physical phenomena [24–27], can be carried out by exploiting the *Fröhlich entropy*. This analysis employs the relationship between  $\epsilon(T)$  and the entropy variation induced by the application of an electric field  $E$  (the probing field in our case) which was provided by H. Fröhlich [28–30]. Fröhlich demonstrated that the entropy variation  $S_E$  of a dielectric subjected to  $E$  is given, for the volume unit, by the relationship

$$S_E = \frac{\epsilon_0}{2} \frac{\partial \epsilon}{\partial T} E^2, \quad (1)$$

where  $\epsilon_0$  is the vacuum permittivity,  $\epsilon$  is the real part of the relative dielectric function in the quasi-static-frequency limit and  $T$  the absolute temperature. It is often useful to consider this last equation for unitary field, which can be written as  $s = S_E/E^2$ , i.e.:

$$s = \frac{\epsilon_0}{2} \frac{\partial \epsilon}{\partial T}, \quad (2)$$

where  $s = s(T)$  is the Fröhlich entropy, for unitary volume and field [22, 29, 31]. Through the relationship 1, Fröhlich pointed out that the application of  $E$  increases the entropy if  $S_E(T) > 0$  and decreases entropy if  $S_E(T) < 0$  [28]. Actually, an external field creates order in a dipolar liquid-like (disordered) system because it orientates some of random-oriented dipoles; the corresponding entropy variation will be negative. On the other hand, in a dipolar ordered system the field increases disorder with a positive value for  $s(T)$  (Fig. S-9). Therefore Fröhlich entropy, through the analysis of the  $\epsilon(T)$ , is able to provide information about the state of order of a dielectric, whose it can be exploited as a useful figure of merit [22, 23, 32]. If an anisotropic dielectric is considered, its relative dielectric response is given by a tensor  $\epsilon_{ij}$ , which is diagonal in the main crystalline axes reference system [34]. In these conditions Eq. (1) becomes

$$S_E = \frac{\epsilon_0}{2} \sum_{ij} E_j \frac{\partial \epsilon_{ij}}{\partial T} E_i, \quad (3)$$

where  $E_i$  and  $E_j$  are the components of the field [29, 33, 34]. Fig. S-10 shows the Fröhlich entropy in each of the three main crystalline axes, i.e. calculated for an electric field with unitary strength in the considered direction. If an electric field with non-zero components along the three main axes is considered, Eq. (3) provides the correlated Fröhlich entropy as the sum of three terms [29, 33–35]. In particular, for an electric field with unitary component along each main axis, so that  $E_x = E_y = E_z$ , relationship (3) becomes  $S_E = (\epsilon_0/2)[(\partial \epsilon_{11}/\partial T)E_x^2 + (\partial \epsilon_{22}/\partial T)E_y^2 + (\partial \epsilon_{33}/\partial T)E_z^2]$ , and its result is depicted in Fig. 3C of the main text. In Figure S-10 Fröhlich entropy curves point out the signature of the above found transitions at 287, 228, and 180 K is displayed, with a trend analogous to that already found for KLTN and KNTN [22, 23]. Similarly to what highlighted in the main text, it is worth observing that in each considered direction, below the highest transition temperature Fröhlich entropy changes its sign from positive to negative, therefore evidencing the onset of a progressive increase of the disorder. If we consider the  $a$  direction (Fig. S-10a and the zoom in Fig. S-11), we note that at lower temperatures an abrupt slowing down of  $S_E$  (i.e. order of magnitude reduction) is displayed at 115 K with the manifestation of strong instability to 110 K, in

correspondence with what observed for  $\epsilon$  in Fig. S-8. Below this temperature,  $S_E$  goes up again and assumes a new uniform trend still remaining until the lowest investigated temperatures. We note that this macroscopic detected transition is fully confirmed by the microscopic diffraction results at about 110-120 K (see Fig. 1A in the main text). In the  $a$ -direction, on the other hand, a clear feature of instability starting at 115 K (Figure S-11) is shown. Subsequently, along this same direction, a broad peak centered at approximately 110 K is found and a change of the  $\epsilon(T)$  curves slope is also observed. This response, though different in shape and intensity with respect to that of the above-considered transformations, can be associated with the occurring structural variations, as shown in XRD measurements.

## SECOND-HARMONIC-GENERATION

The polarization model is illustrated in Fig. 4 of the main. Each cube vortex presents six vortex cores or strings that cross in a central point. Seen along the principal axes, the polarization field is wrapped around each of these cores according to a discrete 2D Heisenberg-magnet like model, forming four separate vortex wings. Seen along, for example, the  $z$  axis (Fig. S-12A), the two wings displaced along the  $x$  direction have a spontaneous polarization along the  $y$  direction, while the two displaced along the  $y$  axis have a polarization along the  $x$  axis. The polarization field in the core itself, that represents a singularity in the distribution, will on average be negligible. Since SHG requires a noncentrosymmetric lattice, a pump field propagating along the core and suffering giant refraction (GR) generates SHG on consequence of the polar structure of the vortex wings. Assuming that the input pump is launched into the vortex core at an angle  $\theta_i$  in the  $x - z$  plane, the TM pump will have the optical field oscillating along the  $x$  axis so that it will lead to an TM-polarized ( $x$ -polarized) SHG from the  $y$  displaced wings, while the  $x$  displaced wings, with a spontaneous polarization orthogonal to the optical polarization, will lead to a negligible SHG signal (Fig. S-12A and Fig. 2B in the main). The opposite will occur for the TE mode (Fig. S-12B and Fig. 2C in the main). In turn, a pump polarized at 45 degrees will lead to two TM and two TE polarized signals that will map the underlying polarization structure of the vortex wings (Fig. 2D in the main). The pump suffers standard GR and exits from the sample at  $\theta_0 = \theta_i$  (Fig. S-12C). The SHG beams are found to propagate from the sample output facet at different characteristic angles that are independent of  $\theta_i$ , forming an angle  $\theta_c$  with the pump, as illustrated in Fig. S-12D for the TM and S-12E for the TE mode. In fact, the pump propagates along the core while the nonlinear susceptibility is laterally displaced along the  $y$  axis for the TM mode and the  $x$  axis for the TE

mode, so that SHG can only form as Cerenkov radiation in conditions of normal dispersion [36]. In turn, while Cerenkov SHG will separate from the pump in a standard material (see S-12A, B), GR causes both pump and SHG, formed as a consequence of the wings, to propagate in the  $z$  direction and only separate on exiting from the sample (see Figs. S-12D, E). The measured angle  $\theta_c = 16^\circ$  is in agreement with coherent Cerenkov SHG radiation for  $n(2\omega) - n(\omega) = 0.045$  [36]. The resulting dispersion  $\Delta n/\Delta\lambda \simeq -0.1(\mu\text{m})^{-1}$  is to be compared with the dispersion  $dn/d\lambda \simeq -0.06(\mu\text{m})^{-1}$  measured independently using group-velocity-dispersion analysis (details not reported here).

## VORTICITY IN SCS

An isolated 3D vortex is associated to 6 independent 2D vortices, i.e., to a set of 6 vorticity pseudovectors ( $\mathbf{v}_1, \dots, \mathbf{v}_6$ ) (red arrows in Fig. 4 main). A 3D vortex with all equal and exiting vorticity components (Fig. 1E left main) will combine into a SC with no resultant strain (“cubic” structure in Fig. 4E main). This is because on each face of the HV unit cell the overall vorticity is zero. For example, consider a HV and its vorticity along the  $a$  direction. The positive  $\mathbf{v}$  encounters an equal and opposite  $-\mathbf{v}$  resulting from its nearest neighbor. Analogously for the  $b$  and  $c$  directions. In turn, a vortex described in Fig. 4D center of the main (“polar” structure) has an anisotropic vorticity set ( $\mathbf{v}_1, \dots, \mathbf{v}_6$ ) with two flipped vorticity vectors along the same axis that, on composing a SC, annul vorticity along the  $b$  and  $c$  directions while increasing it in the  $a$  direction. The “orthorhombic” structure (Fig. 4D right main) is then a product of a SC formed by 3D vortices with only one flipped vorticity.

## VORTEX STRAIN

Barium titanate ( $\text{BaTiO}_3$ ), a prototype for ferroelectric perovskites, undergoes symmetry breaking transitions according to the sequence cubic-tetragonal-orthorhombic-rhombohedral on going from high temperatures to low temperatures. While our experiments confirm this sequence for KTN, single-crystal X-ray diffraction allows the observation of two topologically-driven structural regions, one that manifests an average orthorhombic structure deep inside what would be the tetragonal phase (285-228 K), a second that manifests an average tetragonal structure deep inside what would be the orthorhombic phase (228-182 K). As discussed in Fig. 4 of the main text, the combination of tetragonal solids into a 3D vortex in general leads to an orthorhombic strain field. In turn, if these same solids suffer an orthorhombic distortion associated to the second perovskite phase transition, the same vortex structure is compati-

ble with a tetragonal strain field. In Fig. S-12, the single vorticity component for each face of the 3D vortex is substituted by a set of three different chiral components, and this leads to a tetragonal strain. In the specific representation, a face that in the perovskite tetragonal phase has a strain chiral component along the  $b$  axis will have, in the perovskite orthorhombic phase, a modified component with projections  $(-1,0,-2)$  along the  $(a,b,c)$  directions. The specific model hinges on the fact that the 3D SC is so stable as to survive the second perovskite phase-transition, as suggested by the X-ray data.

---

\* jacopo.parravicini@unimib.it

- [1] Lo Presti, L., Invernizzi, D., Soave, R., & Destro, R., "Looking for structural phase transitions in the colossal magnetoresistive thiospinel  $\text{FeCr}_2\text{S}_4$  by a multi-temperature single-crystal X-ray diffraction study." *Chem. Phys. Lett.* **416**, 28-32 (2005).
- [2] Lo Presti, L., Allieta, M., Scavini, M., Ghigna, P., Locante, L., Scagnoli, V., & Brunelli, M., "Crystal structure and structural phase transitions in the  $\text{GdBaCo}_2\text{O}_{5.0}$  cobaltite," *Phys. Rev. B* **84**, 104107 (2011).
- [3] X.Wang, J.Wang, Y. Yu, H. Zhang, & R. I. Boughton, "Growth of cubic  $\text{KTa}_{1-x}\text{Nb}_x\text{O}_3$  crystal by Czochralski method," *J. Cryst. Growth* **293**, 398-403 (2006).
- [4] Bokov, A.A., "Recent progress in relaxor ferroelectrics with perovskite structure," *J. Mater. Sci.* **41**, 31 (2006).
- [5] B. Zalar, A. Lebar, J. Seliger, R. Blinc, V. Laguta, & M. Itoh, "NMR study of disorder in  $\text{BaTiO}_3$  and  $\text{SrTiO}_3$ ," *Phys. Rev. B* **71**, 0641071 (2005).
- [6] B. Zalar, V.V. Laguta, & R. Blinc, "NMR evidence for the coexistence of order-disorder and displacive components in barium titanate," *Phys. Rev. Lett.* **90**, 037601 (2003).
- [7] A. Agranat, R. Hofmeister, & A. Yariv, "Characterization of a new photorefractive material:  $\text{K}_{1-y}\text{LyT}_{1-x}\text{Nx}$ ," *Opt. Lett.* **17**, 713 (1992).
- [8] A. W. Hewat, "Cubic-tetragonal-orthorhombic-rhombohedral ferroelectric transitions in perovskite potassium niobate: neutron powder profile refinement of the structures," *Journal of Physics C: Solid State Physics* **6**, 2559 (1973).
- [9] J. Toulouse, "The three characteristic temperatures of relaxor dynamics and their meaning," *Ferroelectrics* **369**, 203-213 (2008).
- [10] H. Abe, K. Harada, R. J. Matsuo, H. Uwe, & K. Ohshima, "X-ray diffuse scattering associated with ferroelectric microregions in  $\text{KTa}_{1-x}\text{Nb}_x\text{O}_3$ ," *J. Phys. Cond. Matter* **13**, 3257 (2001).
- [11] S.A. Borisov, S.B. Vakhrushev, E.Yu. Koroleva, A.A. Naberezhnov, P.P. Syrnikov, V.G. Simkin, Z. Kutnjak, T. Egami, W. Dmowski, & P. Piekarczyk, "Investigation into the evolution of the structure of  $\text{K}_{1-x}\text{Li}_x\text{Ta}_{1-y}\text{Nb}_y\text{O}_3$  single crystals under variations in temperature," *Crystallography Reports* **52**, 440 (2007).
- [12] P. M. Gehring, H. Chou, S.M. Shapiro, J.A. Hriljac, D.H. Chen, J. Toulouse, D. Rytz, & L. A. Boatner, "Dipole-glass behavior of lightly doped  $\text{KTa}_{1-x}\text{Nb}_x\text{O}_3$ ," *Phys. Rev. B* **46**, 5116 (1992).
- [13] F. Jona & G. Shirane, *Ferroelectric crystals* (Dover publishing, 1993).
- [14] M. Azuma, W. Chen, H. Seki, M. Czapski, S. Olga, K. Oka, M. Mizumaki, T. Watanuki, N. Ishimatsu, N. Kawamura, S. Ishiwata, M. G. Tucker, Y. Shimakawa, & J. P. Attfeld, "Colossal negative thermal expansion in  $\text{BiNiO}_3$  induced by intermetallic charge transfer," *Nat. Commun.* **2**, 347-352 (2011).
- [15] J. D. Dunitz, "Phase transitions in molecular crystals: looking backwards, glancing sideways," *Physica Scripta* **91**, 112501 (2016).
- [16] Y. V. Mnyukh, "Molecular mechanism of polymorphic transitions," *Mol. Cryst. Liq. Cryst.* **52**, 163 (1979).
- [17] S. Triebwasser, "Study of Ferroelectric Transitions of Solid-Solution Single Crystals of  $\text{KNbO}_3\text{-KTaO}_3$ ," *Phys. Rev.* **114**, 63 (1959).
- [18] Shirane, G., & Takeda, A., "Transition energy and volume change at three transitions in barium titanate," *J. Phys. Soc. Japan* **7**, 1 (1952).
- [19] Rytz, D., & Scheel, H.J., "Crystal growth of  $\text{KTa}_{1-x}\text{Nb}_x\text{O}_3$  ( $0 < x \leq 0.04$ ) solid solutions by a slow-cooling method," *J. Cryst. Growth* **59**, 468 (1982).
- [20] Politova, E. D. , Fortalnova, E. A. , Kaleva, G. M., Mosunov, A. V., Safronenko, M. G., Venskovskii, N. U., Shvartsman, V. V. , & Kleemann, W., "Ferroelectric phase transitions and electroconducting properties of ceramic BIMEVOX solid solutions (Me=La, Zr)," *Ferroelectrics* **391**, 3 (2009).
- [21] V. V. Shvartsman & D. C. Lupascu, "Lead-free relaxor ferroelectrics," *J. Am. Ceram. Soc.* **95**, 1-26 (2012).
- [22] J. Parravicini, E. DelRe, A. J. Agranat, & GB. Parravicini, "Macroscopic response and directional disorder dynamics in chemically substituted ferroelectrics," *Phys. Rev. B* **93**, 094203 (2016).
- [23] Parravicini, J., DelRe, E., Agranat, A.J., & Parravicini, GB., "Liquid-solid directional composites and anisotropic dipolar phases of polar nanoregions in disordered perovskite," *Nanoscale* **9**, 9572-9580 (2017).
- [24] Parravicini, J., Minzioni, P., Degiorgio, V., DelRe, E., "Observation of nonlinear Airy-like beam evolution in lithium niobate," *Opt. Lett.* **34**, 3908-3910 (2009).
- [25] Parravicini, J., Di Lei, F., Conti, C., Agranat, A.J., DelRe, E., "Diffraction cancellation over multiple wavelengths in photorefractive dipolar glasses," *Opt. Express* **19**, 24109-24114 (2011).
- [26] Parravicini, J., Conti, C., Agranat, A.J., DelRe, E., "Rejuvenation in scale-free optics and enhanced diffraction cancellation life-time," *Opt. Express* **20**, 27382-27387 (2012).
- [27] Falsi, L., Tartara, L., Di Mei, F., Flammini, M., Parravicini, J., Pierangeli, D., Parravicini, GB., Xin, F., DiPorto, P., Agranat, A.J., & DelRe, E., "Constraint-free wavelength conversion supported by giant optical refraction in a 3D perovskite supercrystal," *Commun. Mater.* **1**, 76 (2020).
- [28] H. Fröhlich, *Theory of dielectrics*, 2nd ed. (Clarendon Press, Oxford, UK, 1958).
- [29] J. Parravicini, "Thermodynamic potentials in anisotropic and nonlinear dielectrics," *Physica B* **541**, 54-60 (2018).
- [30] G. P. Johari, "Effects of electric field on the entropy, viscosity, relaxation time, and glass-formation," *J. Chem. Phys.* **138**, 154503 (2013).
- [31] P. Tan, H. Tian, F. Huang, X. Meng, Y. Wang, C. Hu, X. Cao, L. Li, & Z. Zhou, "Strain-gradient-controlled dis-

- order dynamics in chemically substituted ferroelectrics,” *Phys. Rev. Appl.* **11**, 024037 (2019).
- [32] A. Sassella, D. Braga, M. Campione, T. Ciabattoni, M. Moret, J. Parravicini, & G.B. Parravicini, “Probing phase transitions and stability of organic semiconductor single crystals by dielectric investigation,” *J. Appl. Phys.* **109**, 013529 (2011).
- [33] L. Landau & E. Lifshitz, *Electrodynamics of Continuous Media* (Pergamon Press, Oxford, UK, 1960).
- [34] J. Nye, *Physical Properties of Crystals - Their Representation by Tensors and Matrices* (Clarendon Press, Oxford, UK, 1985).
- [35] A.F. Devonshire, “Theory of ferroelectrics,” *Advances in Physics* **3**, 85-130 (1954).
- [36] P. K. Tien, R. Ulrich, & R. J. Martin, “Optical second harmonic generation in form of coherent Cerenkov radiation from a thinfilm waveguide,” *Appl. Phys. Lett.* **17**, 447 (1970).
- [37] Due to the very low thermal expansion coefficient of KTN, any thermally induced deformation of the crystal shape while  $T$  is lowered is negligible as well.

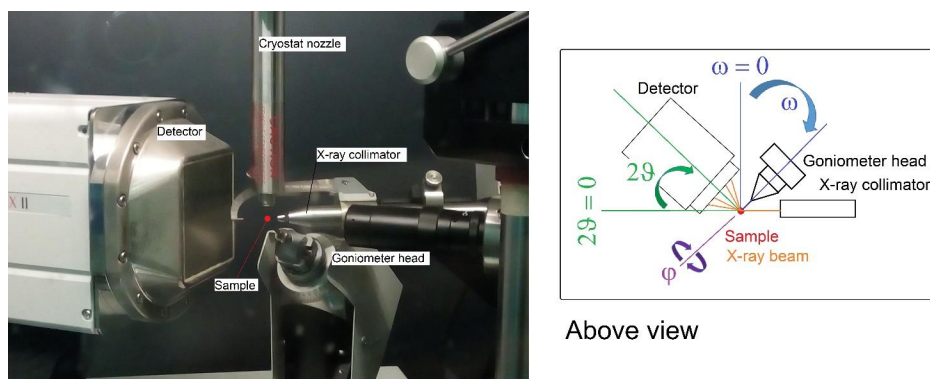


FIG. S-1. The Bruker Smart Apex three-circle goniometer, with operational angles highlighted in the scheme on the right.

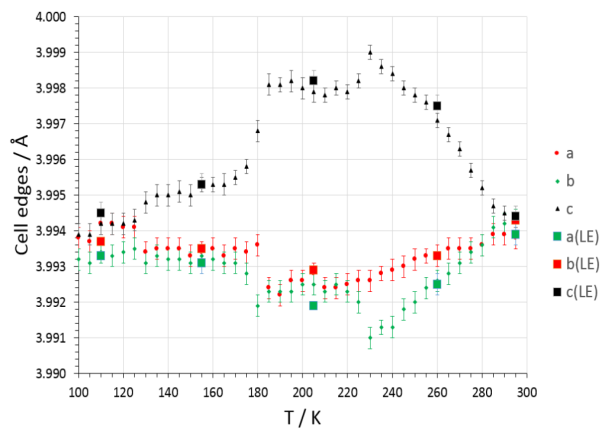


FIG. S-2. Same as Fig. 1 in the main text, with superimposed estimates for the cell parameters after having left the sample free to equilibrate in the cold  $N_2$  stream for several hours (Long Equilibration, LE) as full large squares (green:  $a$ ; red:  $b$ ; black:  $c$ ).

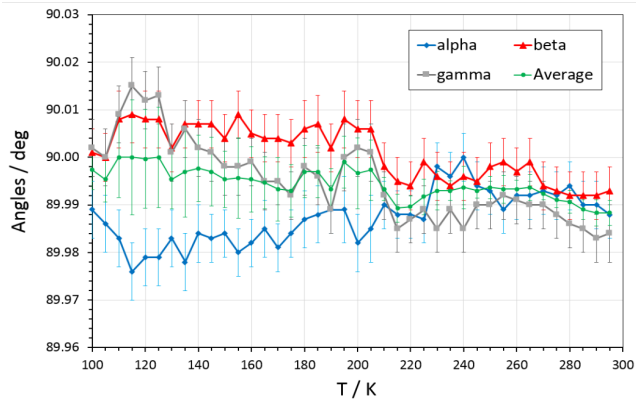


FIG. S-3. Cell angles of KTN as a function of  $T$  for the sample “A”:  $\alpha$  (blue rhombi),  $\beta$  (red triangles),  $\gamma$  (grey squares), together with their unweighted average (green circles). Vertical bars correspond to 1 estimated standard deviation.

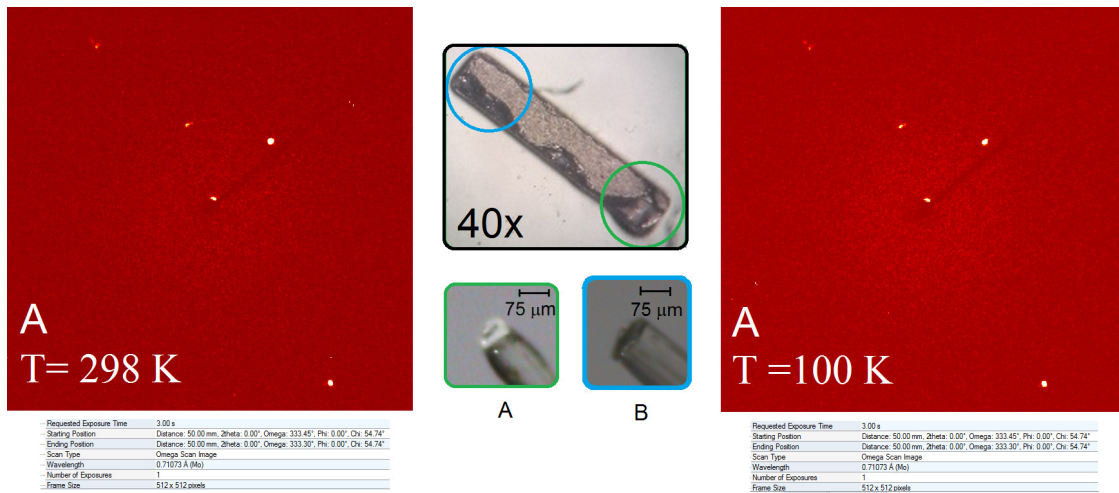


FIG. S-4. Diffraction frame of the KTN crystal “A” at goniometer angles  $2\theta = \phi = 0$ ,  $\omega = -26.7^\circ$  as taken at room temperature (left) and at  $T = 100$  K (right). The material remains fully crystalline in the whole range of  $T$  explored. Inset: picture of the “A” specimen, mounted on the top of a capillary fiber with a drop of bi-component epoxy glue, and of the original rod from which it was cut.

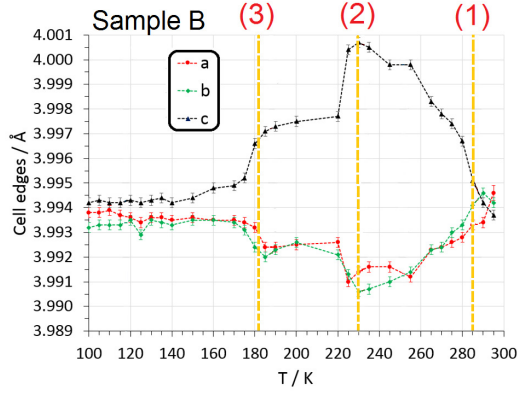


FIG. S-5. Same as Figure 1A in the main text, for the sample B cut from the opposite extremity of the original KTN rod. Changes affecting cell edge lengths ( $\text{\AA}$ ),  $a$  (red dots),  $b$  (green rhombi) and  $c$  (black triangles) are shown as a function of  $T$ . Each point was estimated by SC-XRD from a least-squares fitting against  $\simeq 110$  reflections within  $2\theta \simeq 34^\circ$ . Error bars correspond to 1 estimated standard deviation (e.s.d.). Broken lines serve as eye guides. Vertical dashed lines set phase boundaries of first-order phenomena.

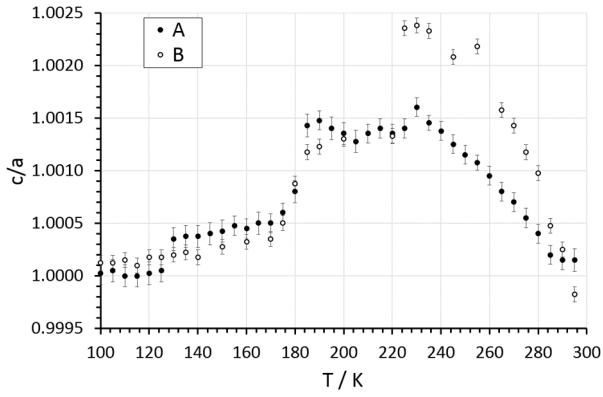


FIG. S-6. Axial ratio  $c/a$  of the KTN unit cell as a function of  $T$ . “A” is the specimen shown in Fig. S-4 (full dots), different from the “B” one (empty dots), cut from the opposite extremity of the as-synthesized KTN rod. Axial ratio  $c/a$  of the KTN unit cell as a function of  $T$ .

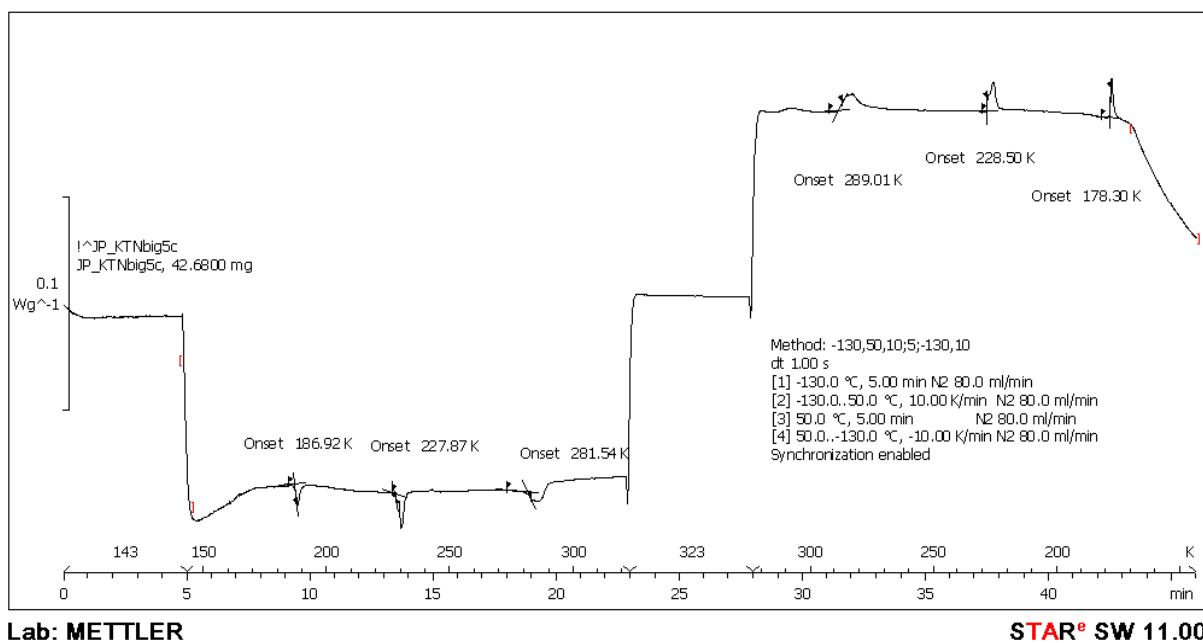


FIG. S-7. DSC trace of KTN crystal undergoing heating and cooling ramps at 10 K/min. Temperature in °C. For clarity, only the onset calculation is shown, but the same peaks were also integrated.

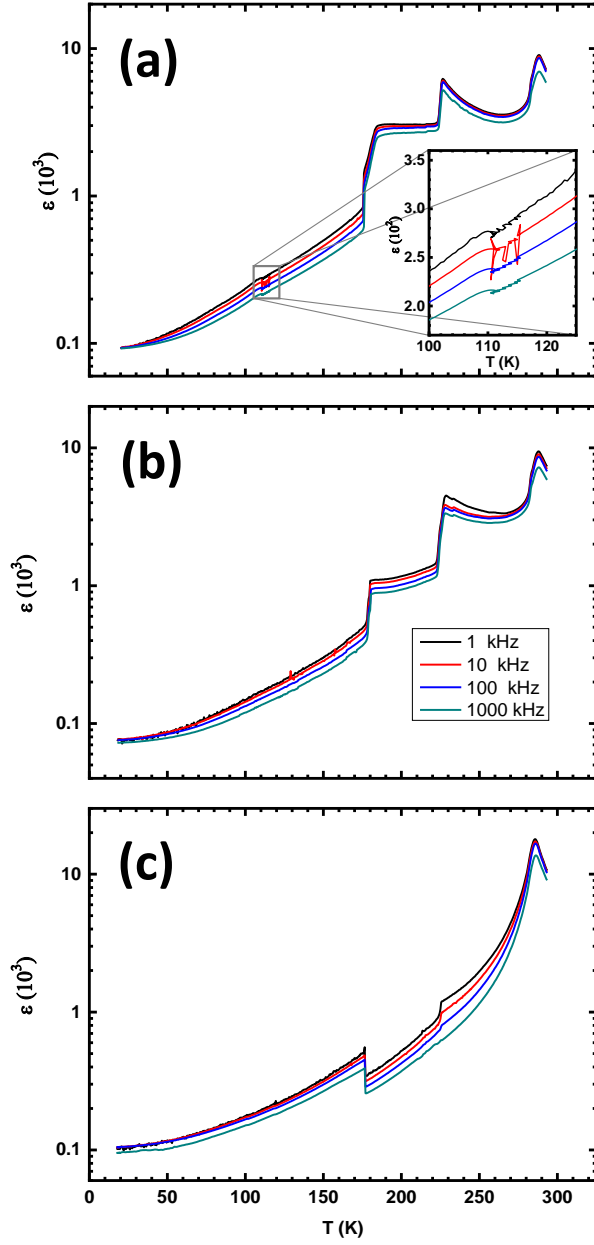


FIG. S-8. Dielectric response as a function of  $T$  along the (a), (b), and (c) main crystalline axes respectively, at the indicated sample frequencies of 1, 10, 100, 1000 kHz. The inset in (a) indicates region of instability.

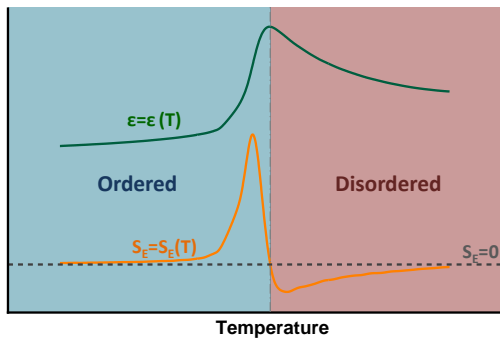


FIG. S-9. From [28]: Schematic temperature dependence of the dielectric constant  $\epsilon$  (blue curve) and of the related entropy change as defined by Eqs. 1 and 2:  $S_E \propto \partial\epsilon/\partial T$  (red curve) due to the field-induced polarization. Fröhlich stated that if  $S_E > 0$  the field creates disorder, while if  $S_E < 0$  it creates order.

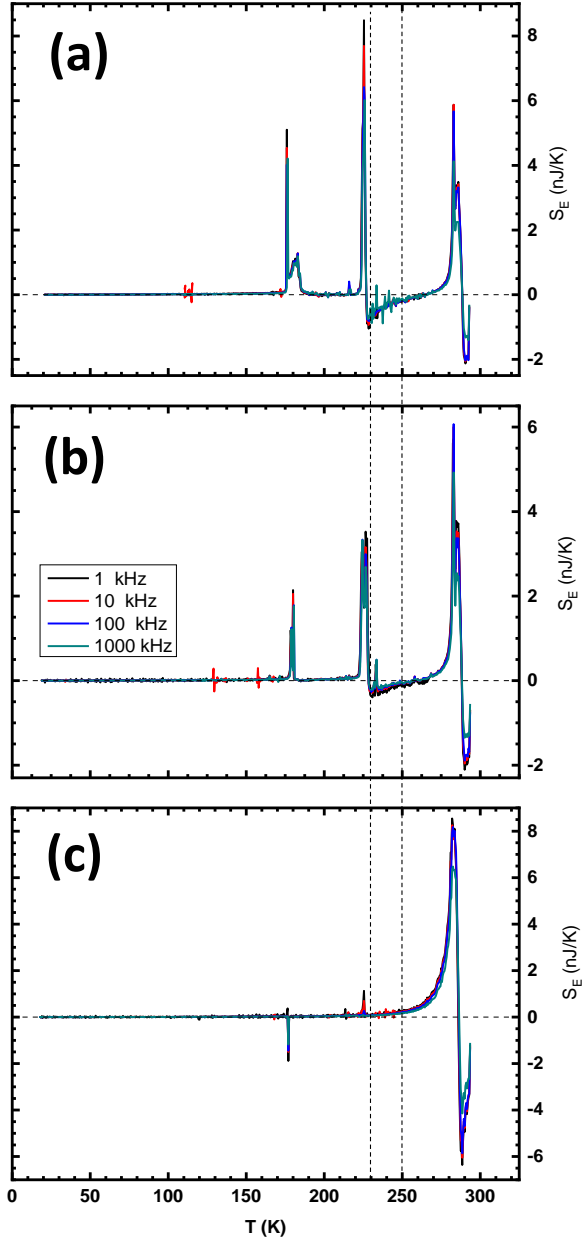


FIG. S-10. Calculated Fröhlich entropy  $S_E = S_E(T)$  (for a unitary electric field) as a function of  $T$  along the (a), (b), and (c) main crystalline axes respectively, at the indicated sample frequencies. Note, in the 230-250 K region the anisotropic order pattern: (a) and (b) directions are disordered, (c) is ordered; also note the oscillations around 115 K, which corresponds to the inset in Fig. S-8a.

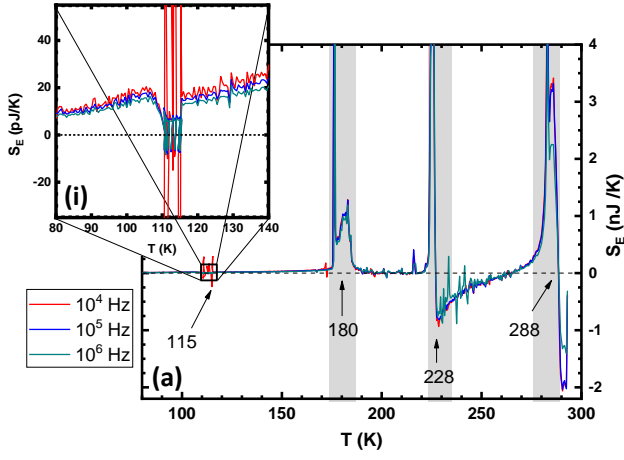


FIG. S-11. Fröhlich entropy in  $a$  direction (the same of the plot in Fig. S-10a) with the transition and instabilities regions evidenced and (i) the relative zoom of the region near 115 K.

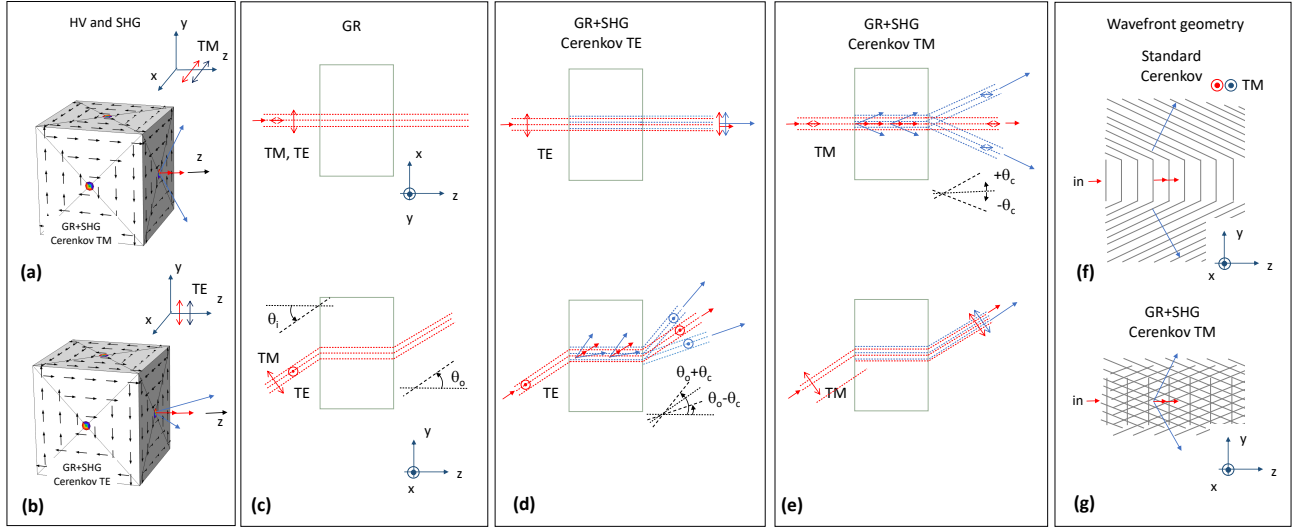


FIG. S-12. GR and Cerenkov phase-matching in a single vortex core (see text).

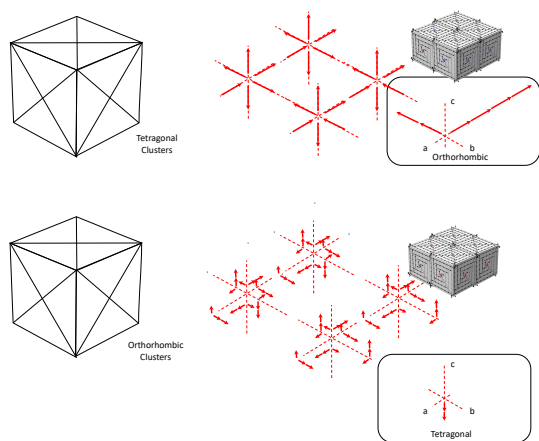


FIG. S-13. Strain produced by a tetragonal 3D vortex (top) leads to an orthorhombic cell, while strain produced by an orthorhombic 3D vortex (bottom) leads to a tetragonal cell.